

Diabatically Induced Secondary Flows in Tropical Cyclones. Part I: Quasi-Steady Forcing

ANGELINE G. PENDERGRASS

Department of Atmospheric Sciences, University of Washington, Seattle, Washington

HUGH E. WILLOUGHBY

Department of Earth Sciences, Florida International University, Miami, Florida

(Manuscript received 20 May 2008, in final form 15 August 2008)

ABSTRACT

The Sawyer–Eliassen Equation (SEQ) is here rederived in height coordinates such that the sea surface is also a coordinate surface. Compared with the conventional derivation in mass field coordinates, this formulation adds some complexity, but arguably less than is inherent in terrain-following coordinates or interpolation to the lower physical boundary. Spatial variations of static stability change the vertical structure of the mass flow streamfunction. This effect leads to significant changes in both secondary-circulation structure and intensification of the primary circulation. The SEQ is solved on a piecewise continuous, balanced mean vortex where the shapes of the wind profiles inside and outside the eye and the tilt of the specified heat source can be adjusted independently. A series of sensitivity studies shows that the efficiency with which imposed heating intensifies the vortex is most sensitive to intensity itself as measured by maximum wind and to vortex size as measured by radius of maximum wind. Vortex shape and forcing tilt have impacts 20%–25% as great as intensity and size, suggesting that the aspects of tropical cyclones that predispose them to rapid intensification are environmental or thermodynamic rather than kinematic.

1. Introduction

One of the most crucial tropical cyclone (TC) forecasting problems is intensification, particularly rapid intensification (RI), where the TC winds increase by more than a Saffir–Simpson category in less than 12 h (AMS 2007; Willoughby et al. 2007). The necessary conditions for RI include low vertical shear of the surrounding wind, a moist lower troposphere, a warm ocean that stays warm, and unrestricted upper-tropospheric outflow. But, in addition, are there aspects of TC structure that predispose them to RI?

To a first approximation, the primary circulations of TCs are warm core, nearly circular vortices in hydrostatic and gradient balance (Shapiro and Willoughby 1982; Willoughby 1990b). Balance is disrupted by strong radial or vertical accelerations. Nonsymmetric

motions are often nonbalanced as well. Nonetheless, a strong, slowly evolving, axially symmetric vortex is a good place to start analysis of tropical cyclone structure and intensity, provided that the analyst recognizes that rapidly changing parts of the flow will generally need to be treated as nonbalanced, perhaps nonlinear, perturbations.

Here, we use the Sawyer–Eliassen equation (SEQ) to revisit the now classical problem of flows induced in balanced vortices by sources of heat or momentum (Smith 1981; Schubert and Hack 1982; Shapiro and Willoughby 1982). The SEQ describes the streamfunction, $\psi(r, z)$, of the secondary flow in the radius–height plane as the vortex evolves slowly, remaining near gradient and in hydrostatic balance. It is derived by the elimination of time and height derivatives of the swirling wind between the thermodynamic energy equation (expressed as a gradient wind tendency equation) and the tangential momentum equation. The result is a Poisson-like equation for the axially symmetric vertical and radial mass flow forced by radial and vertical gradients of the imposed heating and torques, respectively.

Corresponding author address: H. E. Willoughby, Department of Earth Sciences, Florida International University, University Park Campus, PC 344, Miami, FL 33199.
E-mail: hugh.willoughby@fiu.edu

When the vortex is heated locally, ψ describes the rising motion through the locus of the heat source, but also the flow updraft that maintains mass continuity around the heat source. Similarly, cyclonic torques force both radial outflow through the locus of forcing and surrounding, mass-conserving return flow. Although the SEQ is a diagnostic equation, it is not steady state. Substitution of the velocity components deduced from ψ into the thermodynamic and tangential momentum equations allows calculation of the gradual vortex evolution.

In symmetrically stable, balanced vortices, the axially symmetric virtual potential temperature (θ_0) surfaces are nearly horizontal while the absolute angular momentum (Λ) surfaces slope upward relatively steeply as one moves away from the center. The Λ increases outward from the vortex center both because of the Coriolis term and because the swirling wind decreases more slowly than r^{-1} . In still air, as in the stratosphere or outside the vortex, Λ surfaces are vertical cylinders. When the Λ surfaces are packed closely together in radius, the vortex is inertially stable; when the θ_0 surfaces are packed close together in height, the vortex is statically stable. In inertially stable vortices the induced flow is largely vertical and confined horizontally close to the forcing; whereas, in statically stable vortices the induced flow is largely horizontal confined vertically close to the forcing.

This effect is crucial to tropical cyclone intensification because inertial stability is strongest inside the eye where the swirling wind increases outward. Heating in the eyewall induces relatively weak horizontal inflow across the eye boundary. Nonetheless, the wind encounters a sharp angular momentum gradient inside the eye. It induces rapid acceleration of the swirling wind at the radius of maximum wind (RMW) and inward from it, causing the eye to contract as the wind increases. Induced subsidence causes adiabatic warming within the eye, leading to hydrostatic pressure falls that maintain the intensifying wind in gradient balance. Observations (Willoughby et al. 1982; Willoughby 1990a) confirm this *convective ring* model of TC intensification.

Here we reexamine TC intensification as described by the SEQ. We cast the problem in height coordinates, where the horizontal ocean surface is also a coordinate surface. This departure from the usual formulation in mass coordinates, where coordinate surfaces intersect the sea, imposes no more algebraic complexity than use of terrain-following coordinates would. We also use a gradient balance vortex based upon a sectionally continuous wind profile that allows flexible adjustment of the shape of the vortex to test the sensitivity of intensification, particularly rapid intensification, to

vortex structure. The present analysis is also background for a companion paper (Willoughby 2009) that reformulates the SEQ as a circumferential vorticity equation (e.g., Smith et al. 2004; Pearce 2004), which describes responses to time-varying forcing. In the next section we rederive the SEQ. The following two sections explore the properties of the solutions, and in the last section we synthesize the results and draw our conclusions.

2. Analysis

a. Sawyer–Eliassen equation in height coordinates

The Sawyer–Eliassen equation is based upon the axially symmetric tangential momentum (i.e., swirling wind), buoyancy (i.e., thermodynamic energy), gradient balance (i.e., radial momentum), hydrostatic (i.e., vertical momentum), and mass continuity equations for an balanced vortex subject to imposed heating or forces:

$$\frac{\partial v_0}{\partial t} + \zeta u + Sw = M, \quad (1a)$$

$$\frac{\partial b}{\partial t} + Bu + N^2 w = Q, \quad (1b)$$

$$G \equiv \frac{v_0^2}{r} + f v_0 = c_p \theta_0 \frac{\partial \pi_0}{\partial r}, \quad (1c)$$

$$\frac{\partial \pi}{\partial z} = -\frac{g}{c_p \theta_0}, \quad (1d)$$

$$\frac{\partial}{\partial r}(r\rho u) + \frac{\partial}{\partial z}(r\rho w) = 0. \quad (1e)$$

These equations are expressed in cylindrical height coordinates where r is the radius and z is the height; $u(r, z)$, $v_0(r, z)$, and $w(r, z)$ are the radial, tangential, and vertical velocities, respectively; $b(r, z) = g \ln(\theta_0/273.16)$ is the buoyancy, where g is the gravitational acceleration and $\theta_0(r, z)$ is the potential temperature; and $\pi_0(r, z) = (p_0/1000)^{R/c_p}$ is the axially symmetric Exner function, computed from pressure, $p_0(r, z)$, and the gas constant and specific heat at constant pressure for dry air, R and c_p . The swirling wind has vorticity $\zeta = \partial v_0/\partial r + v_0/r + f$ and shear $S = \partial v_0/\partial z$. The radial and vertical gradients of buoyancy are $B = \partial b/\partial r$ and $N^2 = \partial b/\partial z$. The air density is $\rho = 1000\pi^{c_v/R}/R\theta_0$, where c_v is the specific heat of air at constant volume. Here M is the force applied to the air in the tangential direction and $Q = gq/c_p\theta_0$ is the diabatic buoyancy source, where q is the actual heating rate. Note that $\partial B/\partial z = \partial N^2/\partial r$.

Differentiation of (1c) with respect to z produces the thermal wind equation:

$$\frac{\partial G}{\partial z} = \left(\frac{2v_0}{r} + f \right) \frac{\partial v_0}{\partial z} = \xi S \equiv E^2 = B + \gamma N^2, \quad (2)$$

where $\xi = 2v_0/r + f$, $E^2 \equiv \xi S$, $\gamma \equiv G/g$, and (2) may be expressed as

$$\frac{\partial G}{\partial z} = \frac{\partial b}{\partial r} + \gamma \frac{\partial b}{\partial z} = \frac{\partial b}{\partial r} + \frac{\partial(\gamma b)}{\partial z} - \frac{\partial \gamma}{\partial z} b. \quad (3)$$

Multiplying ξ times (1a) forms another expression for $\partial G/\partial t$:

$$\xi \frac{\partial v_0}{\partial t} = \frac{\partial G}{\partial t} = -\zeta \xi u - \xi S w + \xi M = -I^2 u - E^2 w + \xi M, \quad (4)$$

where $I^2 = \zeta \xi$. Note that ξ , I^2 , and E^2 relate to the absolute angular momentum, $\Lambda = rv_0 + fr^2/2$, through $\xi = 2\Lambda/r^2$, $E^2 = r^{-3} \partial \Lambda^2 / \partial z$, and $I^2 = r^{-3} \partial \Lambda^2 / \partial r$.

Differentiating (3) with respect to t and (4) with respect to z , and neglecting terms that contain $\partial \gamma / \partial t$ to be consistent with gradient balance, yields two expressions for the quantity $\partial^2 G / \partial z \partial t$. Algebraic elimination of G combines these expressions into

$$0 = \frac{\partial}{\partial r} \frac{\partial b}{\partial t} + \frac{\partial}{\partial z} \left(\gamma \frac{\partial b}{\partial t} \right) - \frac{\partial \gamma}{\partial z} \frac{\partial b}{\partial t} + \frac{\partial}{\partial z} (I^2 u + E^2 w - \xi M). \quad (5)$$

Substitution from the buoyancy equation, rearrangement, and further substitution from the thermal wind equation transforms (5) into a diagnostic expression in the radial and vertical velocities:

$$\begin{aligned} \frac{\partial}{\partial r} (N^2 w + Bu) - \frac{\partial}{\partial z} (I^2 u + Bw) - \frac{\partial \gamma}{\partial z} (Bu + N^2 w) \\ = \frac{\partial Q}{\partial r} - \frac{\partial}{\partial z} (\xi M) + \gamma \frac{\partial Q'}{\partial z} \end{aligned} \quad (6)$$

where $I'^2 \equiv I^2 - \gamma B$. Representation of the vertical and radial flows with the mass flow streamfunction $\psi(r, z)$ insures mass continuity:

$$u = -\frac{1}{r\rho} \frac{\partial \psi}{\partial z}, \quad w = \frac{1}{r\rho} \frac{\partial \psi}{\partial r}. \quad (7)$$

Substitution into (6) frames a diagnostic equation for the streamfunction:

$$\begin{aligned} \frac{\partial}{\partial r} \left(\frac{N^2}{r\rho} \frac{\partial \psi}{\partial r} - \frac{B}{r\rho} \frac{\partial \psi}{\partial z} \right) + \frac{\partial}{\partial z} \left(\frac{I'^2}{r\rho} \frac{\partial \psi}{\partial z} - \frac{B}{r\rho} \frac{\partial \psi}{\partial r} \right) + \\ \frac{\partial \gamma}{\partial z} \left(\frac{B}{r\rho} \frac{\partial \psi}{\partial z} - \frac{N^2}{r\rho} \frac{\partial \psi}{\partial r} \right) = \frac{\partial Q}{\partial r} - \frac{\partial}{\partial z} (\xi M) + \gamma \frac{\partial Q'}{\partial z} \end{aligned} \quad (8)$$

Finally, defining the vertical and horizontal gradients of density as $H_\rho^{-1} = \rho^{-1} \partial \rho / \partial z$ and $R_\rho^{-1} = r^{-1} + \rho^{-1} \partial \rho / \partial r$, expanding the derivatives, performing some algebra, and collecting terms brings forth:

$$\begin{aligned} N^2 \frac{\partial^2 \psi}{\partial r^2} - 2B \frac{\partial^2 \psi}{\partial z \partial r} + I'^2 \frac{\partial^2 \psi}{\partial z^2} \\ - \left(\frac{N^2}{R_\rho} - \frac{B}{H_\rho} + N^2 \frac{\partial \gamma}{\partial z} \right) \frac{\partial \psi}{\partial r} \\ - \left(\frac{I'^2}{H_\rho} - \frac{B}{R_\rho} - \frac{3\xi S}{r} - N^2 \frac{\partial \gamma}{\partial r} \right) \frac{\partial \psi}{\partial z} \\ = r\rho \left[\frac{\partial Q}{\partial r} - \frac{\partial}{\partial z} (\xi M) + \gamma \frac{\partial Q'}{\partial z} \right] \end{aligned} \quad (9)$$

This version of the SEQ is essentially the same as the conventional form, apart from the terms containing I' or γ . The terms in γ (the ratio of the gradient wind acceleration to the gravity, equal to the slopes of isobaric surfaces) arise because density variations perpendicular to isobaric surfaces are different from those in the vertical (e.g., Smith et al. 2004; Smith 2006). They represent the projection of the isobaric gradient onto the geometric vertical. While (9) is somewhat more complicated than it would be in isobaric coordinates, it is no more complicated than it would be in terrain-following coordinates. Although isobaric coordinates are mathematically suited to this problem, geometric coordinates are more natural for analysis of remotely sensed data (e.g., Roux and Viltard 1995; Viltard and Roux 1998) and avoid intersections of coordinate surfaces with the lower boundary, where the air-sea interactions that drive the cyclone happen.

Here we solve (9) with the Lindzen-Kuo (1969) algorithm for specified M , Q , and the vortex structure. The domain in the r - z plane extends vertically from the surface to 20 km and radially from the vortex center to 1500 km. Vertical and horizontal grid resolutions are 1 and 2 km, respectively. We impose Neumann boundary conditions, $\psi = 0$, at $z = 0$, $z = 20$ km, and $r = 0$, such that there is no axially symmetric flow into the ocean surface, across the center, or out of the top of the domain. We impose a Dirichlet boundary condition, $\partial \psi / \partial r = 0$, at $r = 1500$ km, such that flow into or out of the domain at the distal boundary is strictly horizontal. Surface friction, when active, is modeled by setting $M_D = -c_D |v_0| v_0$ at $z = 0$. The finite differencing of M_D on the right-hand side of (9) forces ψ at the first interior point that sustains inflow over the depth of the lowest mesh interval. This inflow advects angular momentum inward at a rate sufficient to balance the angular momentum lost to the sea through friction. Similar formulations are traditional in studies such as this

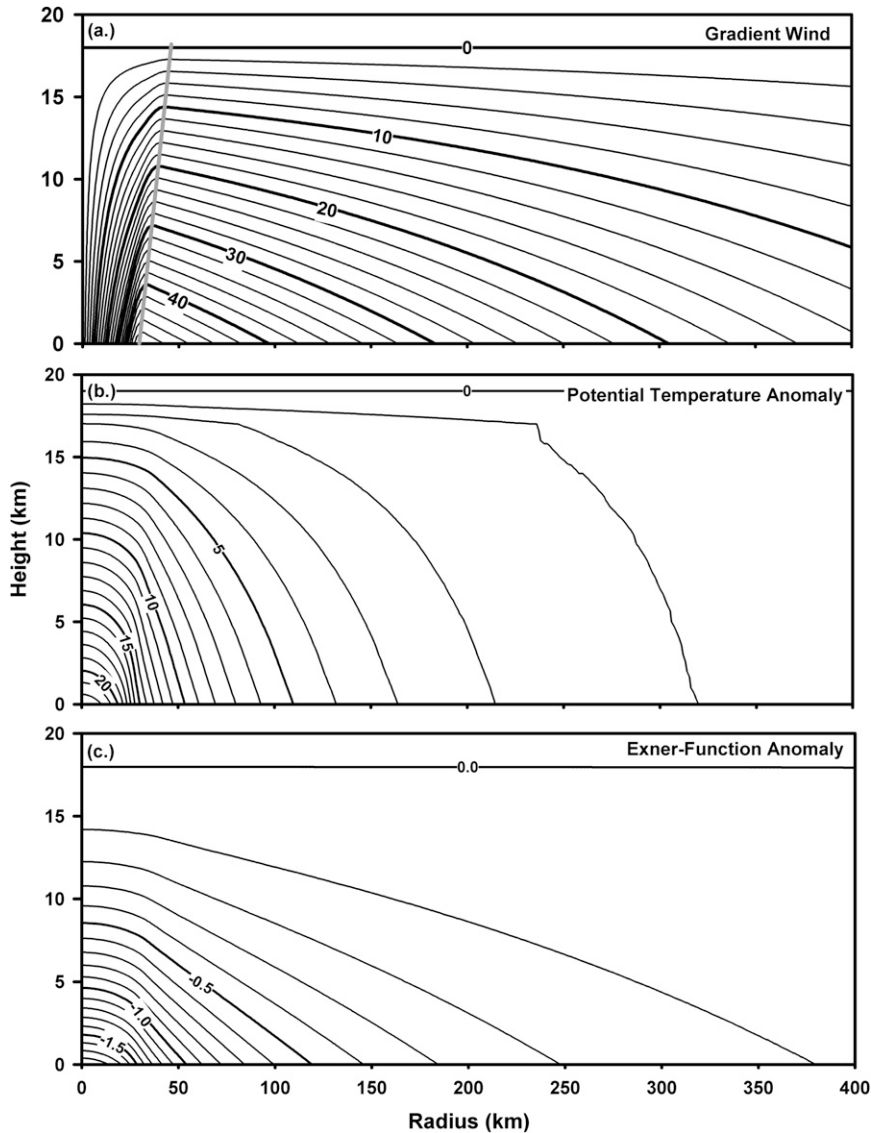


FIG. 1. The idealized vortex with linear wind variation as a function of height: (a) gradient wind (m s^{-1}) computed from (12) with $V_{\text{max}} = 50 \text{ m s}^{-1}$, $R_{\text{max}} = 50 \text{ km}$, $n = 1$, and $X_1 = 300 \text{ km}$; (b) hydrostatically balanced potential temperature anomaly (K); and (c) gradient balanced Exner function anomaly (dimensionless). The sloping gray line in (a) indicates the radius of maximum wind.

(e.g., Ooyama 1969) even though they account for neither the radial component of the drag, which would affect gradient balance, nor the contribution of the radial flow to the magnitude of the wind in the bulk aerodynamic formula, which would increase the frictional torque (e.g., Smith 2003). This simple treatment of the lower boundary condition and surface exchanges justifies the added effort to reformulate the SEQ in height coordinates.

b. Effect on the swirling flow

As mentioned previously, substitution of the forced u and w into (1a) and (1b) affords a way to calculate the

evolution of the vortex in response to imposed forcing. When the forcing in (1) is too strong for gradient balance, departures from the gradient wind arise (e.g., Roux and Viltard 1995; Zhang et al. 2000). Provided that the forcing is not too strong, the agradient swirling wind can be calculated from the linearized form of the radial momentum equation that includes the advective terms (e.g., Bister and Emanuel 1998; Emanuel 2004) neglected in (1c):

$$\frac{\partial u}{\partial t} + u \frac{\partial u}{\partial r} + w \frac{\partial u}{\partial z} - \xi v' = 0, \quad (10)$$

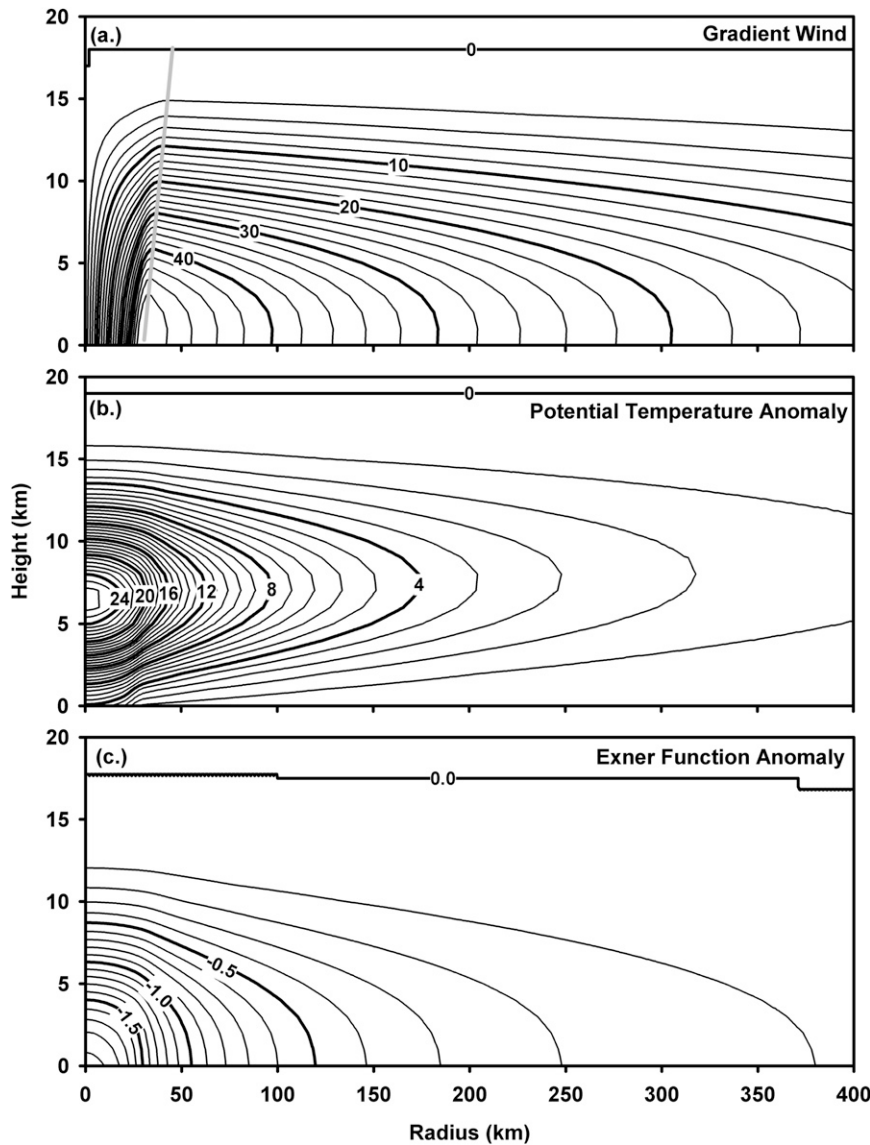


FIG. 2. As in Fig. 1, but for the realistic vortex with ramp function vertical structure.

where v' is the perturbation to the gradient wind and u and w are deduced from ψ . Here, accelerations of the forced secondary flow affect the linearized departure from balance much as modifications to the radial pressure gradient would. If we neglect time changes to be consistent with gradient balance of the underlying vortex and add and subtract $w\partial w/\partial r$, (10) rearranges to

$$\xi v' = \frac{\partial}{\partial r} \left(\frac{u^2}{2} + \frac{w^2}{2} \right) - w \left(\frac{\partial w}{\partial r} - \frac{\partial u}{\partial z} \right). \quad (11)$$

The first term on the right is the radial gradient of secondary-circulation kinetic energy and the second is

the radial “Coriolis force” due to the cross product of the circumferentially directed component of the secondary-circulation relative vorticity and the axially symmetric vertical velocity. For example, when the radial flow decelerates inward, as in the convergence to feed the eyewall updraft, or when the inflow decreases upward as it emerges from the boundary layer to join and updraft, (11) indicates that the swirling wind should be supergradient.

c. Balanced vortex

The balanced primary circulation is based on an empirically derived sectionally continuous algebraic profile

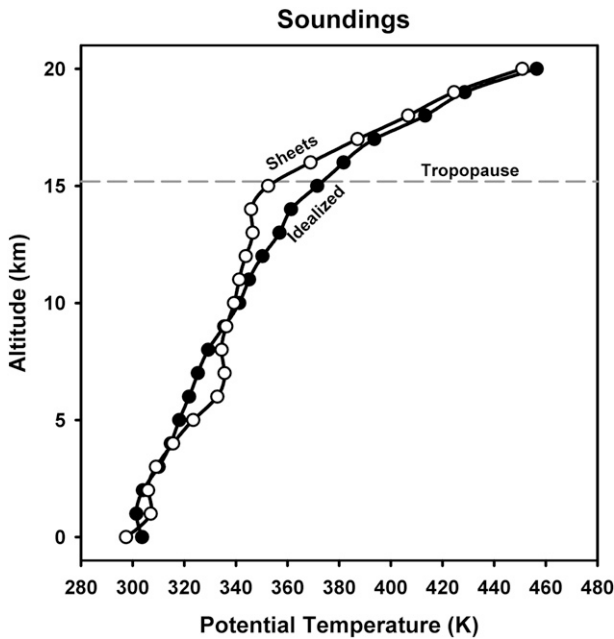


FIG. 3. Potential temperature (K) as a function of height in the Sheets (1969) and idealized constant lapse rate (CLR) environmental soundings.

(Willoughby et al. 2006). Its horizontal structure is composed of analytical segments patched smoothly together. Inside the eye, the wind is proportional to a power of radius, n . Outside the eye, the wind decays exponentially with an e -folding distance, X_1 . These profiles are patched together across the radius of maximum wind using a smooth polynomial ramp function:

$$v_0(r, z) = V_i = V_{\max}(z) \left[\frac{r}{R_{\max}(z)} \right]^n, \quad 0 \leq r \leq R_1(z), \quad (12a)$$

$$v_0(r, z) = V_i[1 - A(x)] + V_o A(x), \quad R_1(z) \leq r \leq R_2(z), \quad (12b)$$

and

$$v_0(r, z) = V_o = V_{\max}(z) \exp \left[-\frac{r - R_{\max}(z)}{X_1} \right], \quad R_2(z) \leq r. \quad (12c)$$

Here V_i and V_o are the swirling wind inside the eye and beyond the transition zone, which lies between $r = R_1(z)$ and $r = R_2(z)$; $V_{\max}(z)$ and $R_{\max}(z)$ are the maximum wind and radius at which the maximum wind occurs, respectively. Note that both V_i and V_o are defined throughout the transition zone and that both are equal to $V_{\max}(z)$ at $r = R_{\max}(z)$. The weighting function, $A(x) = 10x^3 - 15x^4 + 6x^5$, is a polynomial ‘‘Bellramp’’ function that varies smoothly from 0 to 1 between R_1

and R_2 as a function of its argument $x = (r - R_1)/(R_2 - R_1)$, which varies linearly from 0 to 1 over the same interval. By definition, $A(x)$ is 0 for $x \leq 0$ and 1 for $x \geq 1$. In summary, (12) defines the swirling wind as an increasing power law inside the RMW and a decreasing exponential function outside the RMW. In a transition region that spans the RMW, it is a spatially varying weighted sum of the inner and outer profiles with continuous first through third derivatives.

The mass field in balance with this vortex is calculated numerically by integrating (1c) inward from an environmental sounding specified as a function of height at the vortex periphery, holding θ_0 constant with the value in the outer sounding at each altitude. The result is an approximate field of π_0 . We then adjust θ_0 toward hydrostatic equilibrium using (1d) and iterate the radial and vertical integrations once or twice to convergence, yielding fields of the Exner function and potential temperature in gradient and hydrostatic balance with wind specified by (12a)–(12c).

We use two vertical structures: the idealized vortex (IV), where $V_{\max}(z)$ decreases linearly with height from the surface to 18 km (Fig. 1), and a ‘‘realistic’’ vortex (RV), where $V_{\max}(z)$ is a lower-order Bellramp function so that vertical shear is concentrated in the upper troposphere rather than spread uniformly from the surface to the tropopause (Fig. 2). In both vortices, R_{\max} slopes outward 16 km from the surface to the top of the vortex at 18-km altitude (e.g., Jorgensen 1984) and we use an idealized environmental sounding (Fig. 3) in which the temperature decreases from 300 K at the surface to 200 K at tropopause level, 15 km. In the stratosphere, the temperature is isothermal at 200 K. We have also experimented with a mean observed sounding in the hurricane environment (Sheets 1969), but its low static stability (*slower* increase of θ with height) in the upper troposphere placed restrictive limits on V_{\max} for symmetrically stable ($N^2 l^2 - B^2 > 0$) vortices.

The baseline vortex shown in these figures is specified by $V_{\max}(0) = 50 \text{ m s}^{-1}$, $R_{\max}(0) = 30 \text{ km}$, $n = 1.0$, and $X_1 = 300 \text{ km}$ for both IV and realistic RV. In IV, the warm anomaly is artificially concentrated at the surface and decreases upward. In RV, the warm anomaly is in the upper troposphere, but not as high as observations indicate (e.g., La Seur and Hawkins 1963). These difficulties with symmetric instability and the altitude of the warm anomaly suggest that real hurricane circulations may extend farther into the stratosphere than is generally appreciated. For most experiments, we use IV because it produces less complicated forced flows and remains symmetrically stable to higher wind speeds. The realistic vortex provides additional insights into the role of static stability.

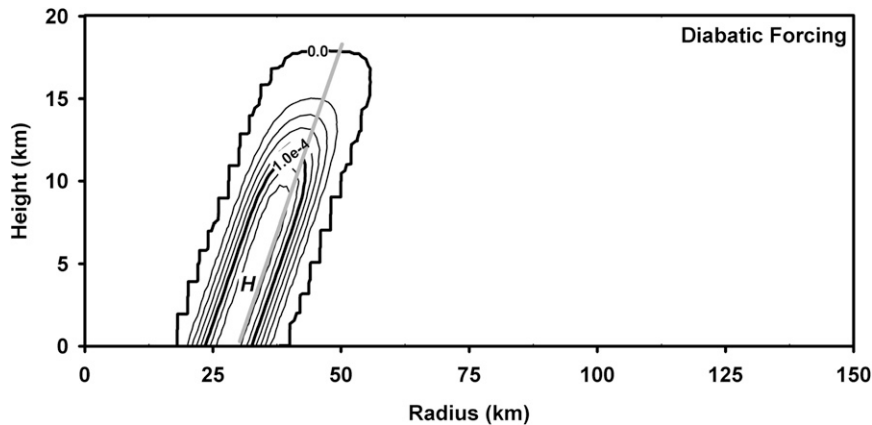


FIG. 4. Outwardly sloping heat source nominally scaled to produce 1 m s^{-1} vertical velocity in the lower troposphere at the radius of maximum winds.

3. Forced circulations

Here we apply the analysis of section 2 to radial and vertical secondary flows forced by specified heat sources and consider the effect of a surface momentum sink. The heat source is either an outward-sloping locus of convective heating centered just inside $R_{\text{max}}(z)$ or an outer convective ring. The momentum sink is represented as bulk aerodynamic surface drag. The axis of the eyewall heat source Q is parallel to the RMW, 2 km inside it, consistent with the observational analysis by Jorgensen (1984). Its radial structure is modeled with a finite-width polynomial Bell function (Willoughby et al. 2006); its vertical structure is modeled with the same ramp function used in construction of the mean vortex (Fig. 4). Its magnitude is scaled to produce a 1 m s^{-1} updraft with lower-tropospheric static stability ($w = Q/N^2 = 1 \text{ m s}^{-1}$). The heat source extends to the top of the vortex at 18 km, 3 km above the tropopause.

Applied to the IV, this forcing induces a streamfunction dipole that straddles the RMW (Fig. 5). The streamfunction gyres are centered in the lower troposphere. The minimum is just inside the eyewall (Fig. 5a) at about 2-km altitude, and the maximum is just outside the eyewall at 4 km. Streamlines converge into the locus of heating at low levels, are tightly packed between the gyres and diverge above 6 km.

The vertical velocity (Fig. 5b) exhibits $>1.2 \text{ m s}^{-1}$ ascent along the axis of the heat source. Weak descent (about 20 cm s^{-1}) flanks the updraft on both sides, consistent with the response to a point heat source (Shapiro and Willoughby 1982). Weaker descent fills the eye below 13 km, as in observed hurricane eyes (e.g., Willoughby 1998). Outside of the eye, there is weak descent ($<1 \text{ cm s}^{-1}$) below 7–10 km and weak ascent

above (1 mm s^{-1} to 1 cm s^{-1}). This pattern is similar to observed patterns of mesoscale vertical motion in hurricanes (Marks and Houze 1987), but here it arises from only the diabatic forcing in the eyewall without hydrometeor evaporation, melting, or ice deposition in the upper-tropospheric anvil that spreads from the anvil in nature.

Horizontal outflow from inside the eye and inflow from outside the eye converges into the updraft below 2 km (Fig. 5c). Above 2 km, outflow extends from just inside the sloping RMW outward. It peaks in the eyewall at $>3 \text{ m s}^{-1}$ near 11 km. This outflow is about 10 km deep, but the strongest wind outside the eyewall is concentrated between 12- and 14-km altitude. It decreases with distance from the RMW, but is still $>1 \text{ m s}^{-1}$ at 140-km radius. Inside the eyewall, from 3- to 14-km altitude, inflow converges from the main updraft into the eye, with a maximum of 0.5 m s^{-1} at 7 km. Outside the eye, there is a deep inflow layer below 5–6 km that maintains speeds greater than 1 m s^{-1} beyond a 50-km radius. This is the thermally forced deep inflow that advects angular momentum to spin up the vortex (Ooyama 1982). Outside the eye, gradual descent partially compensates for the inward angular momentum advection by downward advection of low Λ air from aloft.

The IV's simple structure provides easy-to-interpret results, but the RV is closer to observed hurricanes. The two cases differ largely in static and inertial stability. The RV is barotropic near the surface and baroclinic only in the middle and upper troposphere. As a result, it is less statically stable above the maximum mean buoyancy. The eyewall streamfunction dipole is higher than in the IV (Fig. 6a). Its maximum is at 8-km altitude

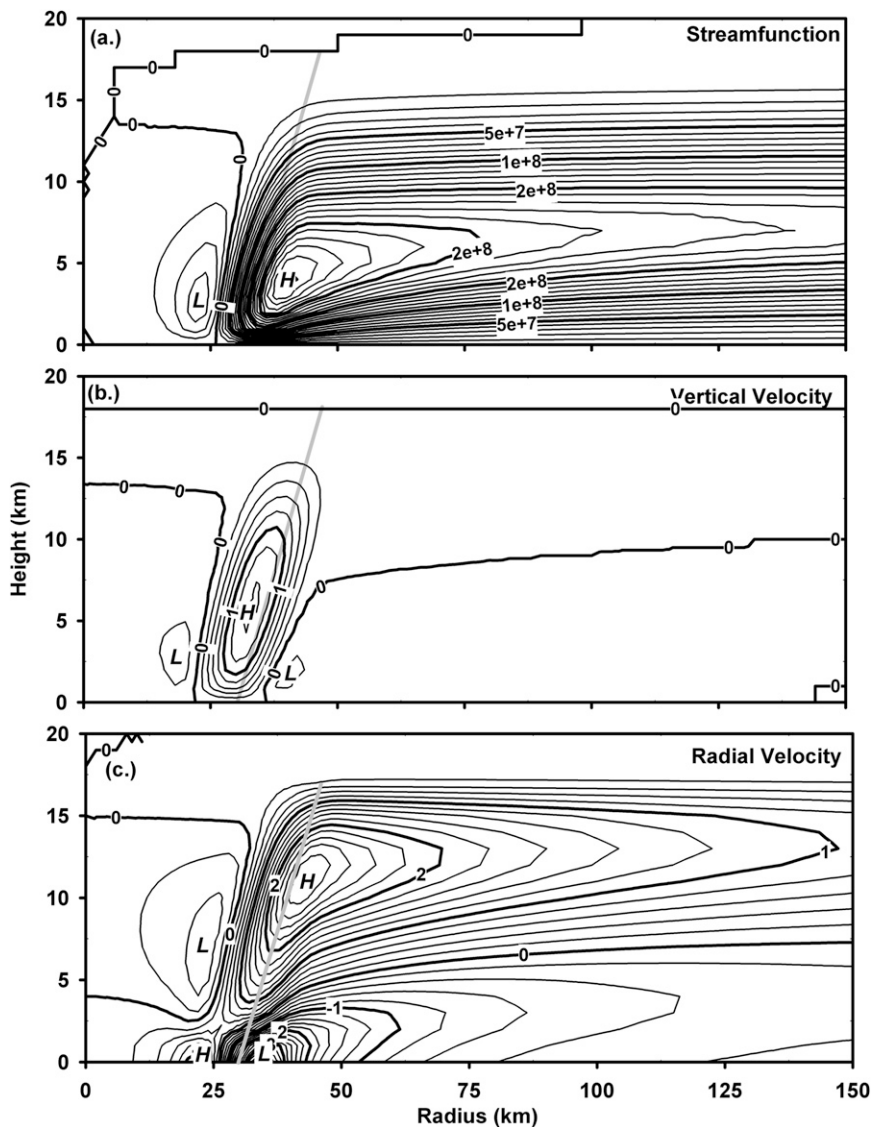


FIG. 5. Secondary circulation induced by the specified heat source acting on the idealized vortex: (a) mass flow streamfunction (kg s^{-1}), (b) vertical velocity (m s^{-1}), and (c) radial velocity (m s^{-1}).

outside the eyewall, and its minimum is at 10 km inside, with a tight gradient across the RMW between. Below 8 km, the streamfunction contours converge toward the eyewall and turn upward from about 40-km radius. Within the eyewall, contours are vertically oriented below 5 km in the low-level barotropic swirling flow, and slope outward at higher levels where the flow is baroclinic.

The vertical motion in the RV reaches a maximum of more than 2 m s^{-1} in the RMW at 9–10-km altitude (Fig. 6b). The maximum descent (40 cm s^{-1}) is at 10–11-km altitude, just inside the eye. The upper-level ascent and lower-level descent are similar to the IV. Outside

the eyewall, inflow extends from the surface to just below 10 km (Fig. 6c), but it is much weaker than in the IV case. Strong inflow (2 m s^{-1}) centered at 35-km radius feeds the updraft, but there is little low-level outflow from the eye. Compared with the IV case, the upper-tropospheric outflow is half as deep, 1 to 2 km higher, and 3 times as strong, maintaining speeds greater than 2 m s^{-1} beyond the 140-km radius. At least some of this additional speed is due to decreased density at the higher outflow altitude. Inside the eye, there is a 2 m s^{-1} inflow maximum at 12-km altitude. From 4 to 10 km in the eye, coincident with the enhanced stability below the midlevel buoyancy maximum, there is strong

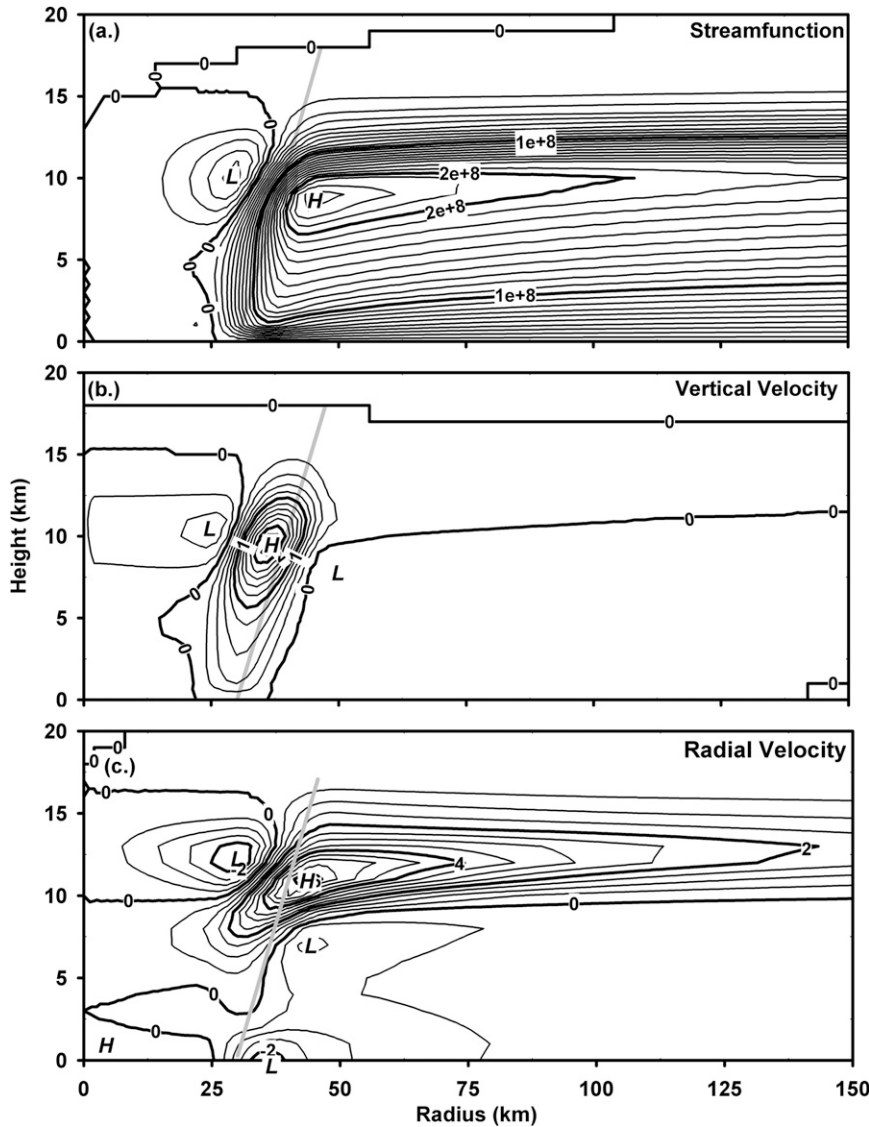


FIG. 6. As in Fig. 5, but for the realistic vortex.

outflow. This altitude is also where descent from the upper troposphere meets ascent from below. Willoughby (1998) reported inversions in the eyes of hurricanes and concluded that they separate upper-level descent from lower-level ascent. The results here suggest that this level is the locus of outflow, though the boundary here is higher than the inversions observed in that study (1–3 km). The differences between the RV and IV arise from vertical changes in stability due to the buoyancy stratification from the elevated warm potential temperature anomaly. In the RV, the increased static stability below the midlevel potential temperature anomaly spreads the acceleration of the updraft vertically, leading to deeper but weaker inflow.

In the IV, the forced secondary circulation changes the primary vortex through balanced tendencies of tangential wind and Exner function and also forces supergradient tangential wind. The tangential wind perturbation from gradient wind (Fig. 7a) is an outward-sloping cone of $\sim 1 \text{ m s}^{-1}$ supergradient winds along the axis of the heat source. It is forced by the radial gradient of secondary-flow kinetic energy and secondarily by the product of w with the tangential vorticity in (11). There is a small area of subgradient wind near the 38-km radius where inflow accelerates toward the eyewall, resulting in an inward increase in secondary-circulation kinetic energy.

Balanced acceleration of the primary flow is strongest at the surface and extends up the inside of the eyewall to

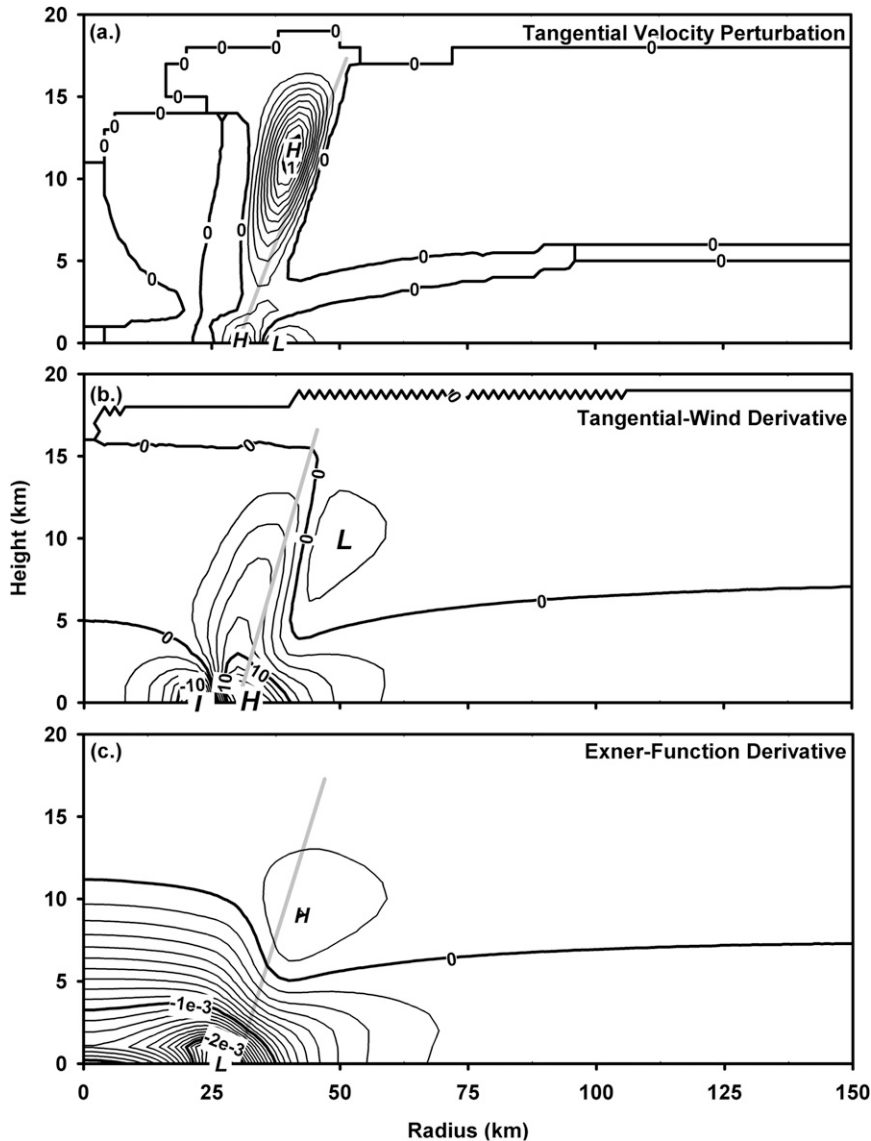


FIG. 7. Idealized vortex responses to forcing: (a) a gradient swirling wind (m s^{-1}), (b) swirling wind tendency ($\text{m s}^{-1} \text{h}^{-1}$), and (c) Exner function tendency (h^{-1}).

the tropopause (Fig. 7b). This acceleration is primarily caused by upward and inward advection of angular momentum. It represents contraction of the eye as described by Schubert and Hack (1982), Shapiro and Willoughby (1982), Schubert et al. (2007), and Willoughby (1990a). Inside the eye at low levels, there is strong deceleration due to thermally forced outflow. This causes the profile to become more U-shaped (as in Willoughby 1998) over time. Outside the eye above 5 km, there is a slow weakening of the swirling wind due to outward advection of low angular momentum in the deep outflow.

The Exner function falls throughout the eye from the surface to between 7 and 11 km in gradient balance with

the swirling wind, as described in the above references (Fig. 7c). The Exner function fall is strongest at the surface where the wind increases the fastest. A weak Exner function rise straddles the RMW at 9-km altitude at the inward edge of the weakening swirling wind, and it extends into the eye despite weakly increasing wind there.

In the RV, the forced secondary circulation induces more complicated changes. Supergradient swirling winds are concentrated in the upper troposphere (Fig. 8a). Maximum values of 5 m s^{-1} occur at 11-km altitude where the outflow accelerates most sharply. Subgradient winds of 2 m s^{-1} occur just inside the eye at 12-km altitude where inflow accelerates inward, but become

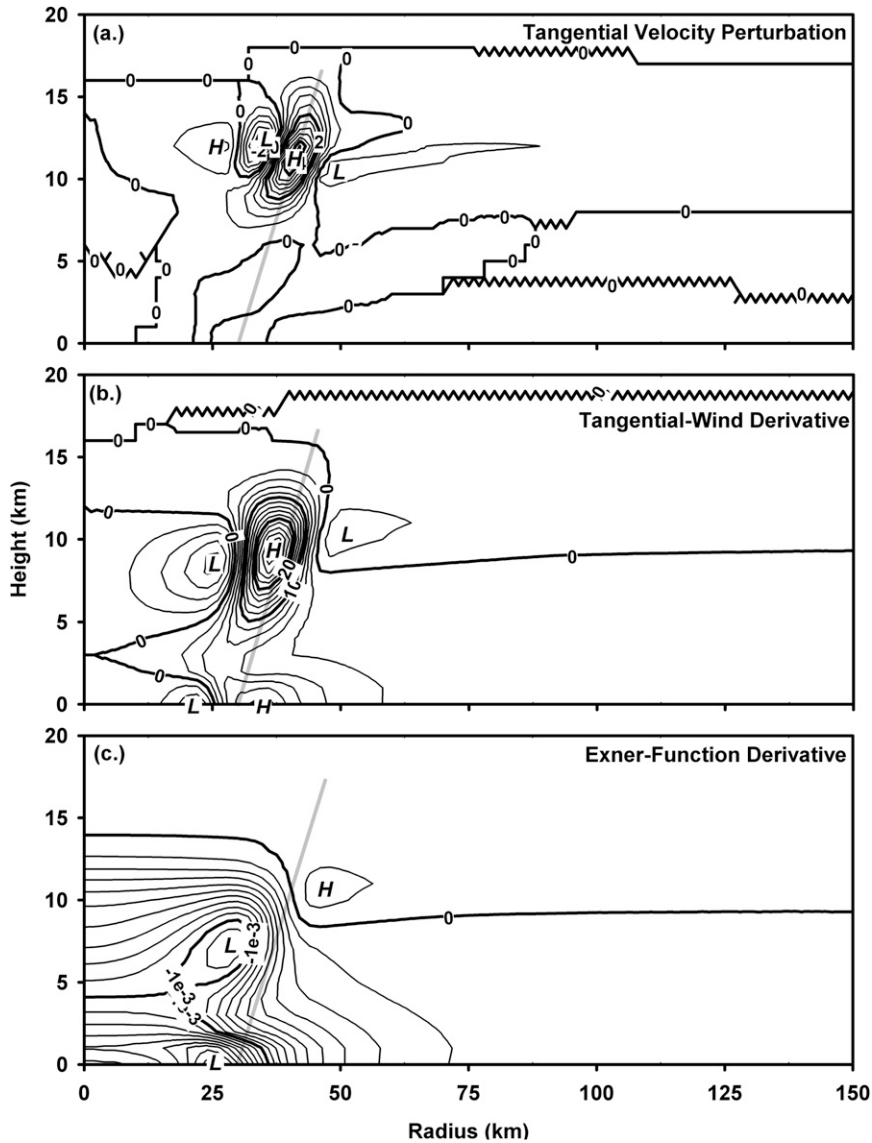


FIG. 8. As in Fig. 7, but for the realistic vortex.

supergradient as the inward secondary flow decelerates near the center.

The increases of the primary tangential wind (Fig. 8b) also occur primarily at upper levels. The maximum, $30 \text{ m s}^{-1} \text{ h}^{-1}$, is centered at 10-km altitude. It is 2–3 times stronger than in the IV. The swirling wind weakens inside the RMW, except at 3 km (just below the θ_0 maximum), where inflow enters the eye, penetrates almost to the center, and then turns outward. The maximum rate of weakening is $6 \text{ m s}^{-1} \text{ h}^{-1}$ at about 8-km altitude. In the upper-tropospheric outflow outside the eye, the wind also weakens slowly.

In the RV, balanced Exner function falls (Fig. 8c) inside the eye extend to 14-km altitude. The strongest falls are

just inside the eye near 8-km altitude and at the surface. Outside the eye above 9 km and inside the eye above 14 km, weak Exner function rises fill the upper troposphere, coincident with weakening of the swirling wind.

4. Sensitivity

To assess aspects of tropical cyclone structure that favor rapid intensification, we explore sensitivity of swirling wind and Exner function tendencies to V_{max} and R_{max} , vortex shape (n and X_1), and tilt and location of heat source. We also consider the effect of bulk aerodynamic surface friction. The measures used are the maximum tangential wind tendency, $(\partial v_0 / \partial t)_{\text{max}}$, and

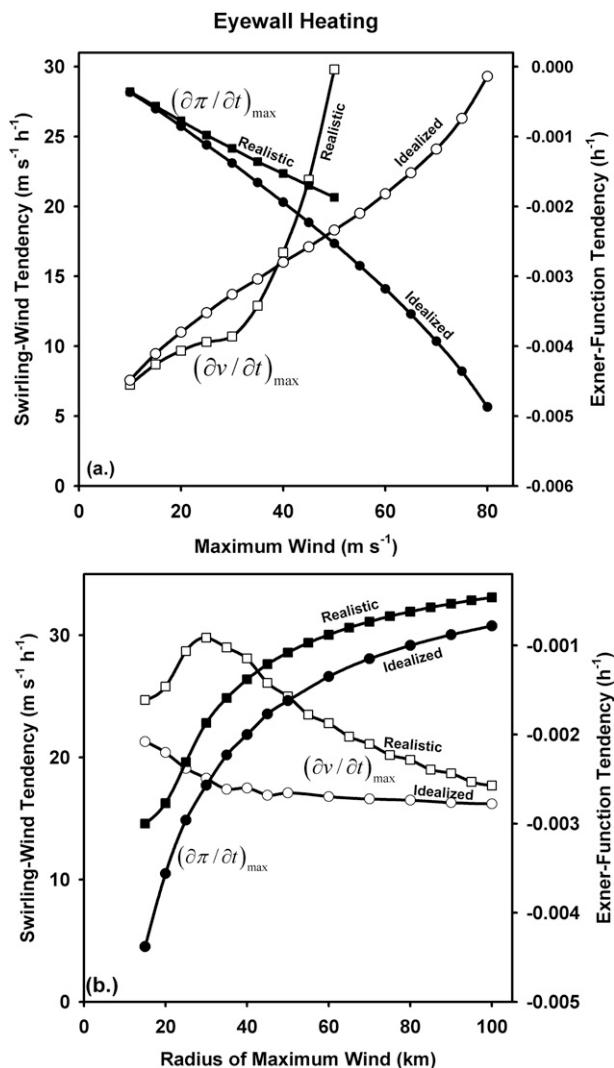


FIG. 9. Maximum rates of change of swirling wind and Exner function as functions of (a) maximum swirling wind and (b) radius of maximum wind for calculations as shown in Figs. 7 and 8.

the minimum Exner function tendency, $(\partial\pi/\partial t)_{\min}$, anywhere in the vortex. If $(\partial v_0/\partial t)_{\max}$ is at the RMW, and if $(\partial\pi/\partial t)_{\min}$ is at the minimum π , then these derivatives represent intensification rates. In cases when $(\partial v_0/\partial t)_{\max}$ is inside (outside) the RMW, then some of the wind tendency contributes to contraction (expansion) of the RMW. Taken together, these measures are an indication of the efficiency with which imposed heating can intensify a given vortex.

a. Sensitivity to V_{\max} and R_{\max}

Eyewall heating, scaled and positioned as described above, causes more rapid strengthening of the swirling wind and more rapid Exner function falls as the maximum tangential wind increases (Fig. 9a). The RV has

larger maximum swirling wind tendencies than the IV because the largest tendencies are in the upper troposphere where the secondary circulation is stronger due to the lower air density aloft. The sudden increase in swirling wind tendency between V_{\max} of 35 and 40 m s^{-1} occurs when the location of the maximum migrates from the surface to the upper troposphere. Exner function falls are weaker in the RV because they extend vertically throughout the eye, instead of being concentrated near the surface. The RV becomes symmetrically unstable for maximum swirling wind over 55 m s^{-1} , while the IV remains symmetrically stable for $V_{\max} \leq 80 \text{ m s}^{-1}$.

Maximum wind tendency and Exner function fall increase as RMW decreases (Fig. 9b) for both vortices, in agreement with Schubert and Hack (1982), Shapiro and Willoughby (1982), and Smith (1981). Maximum tangential wind speed is 50 m s^{-1} for all values of RMW. These changes reflect more efficient intensification as the local Rossby radius of deformation decreases relative to the RMW. Measured in terms of swirling wind, the RV intensifies more rapidly for all values of R_{\max} , again because the largest changes are in the upper troposphere. Maximum tendencies are relatively insensitive to the radius of maximum wind when it is $>40 \text{ km}$ because R_{\max} is much greater than the local Rossby radius.

To summarize, the intensification rate increases as the eye becomes smaller and the maximum wind increases. Because V_{\max} increases and R_{\max} decreases in intensifying TCs, the rate of intensification for fixed heating increases with increasing intensity if the vortex shape defined by n and X_1 remains the same. Of course, the spatial structure of the computed tangential wind tendency does not support fixed shape. But these results imply a positive feedback during intensification. Eyewall heating causes strengthening of the primary vortex and contraction of the eye, which make further intensification more efficient. In nature, however, as intensifying TCs approach their maximum potential intensity (MPI), the heating rate diminishes, causing the intensity to asymptote to the MPI despite greater efficiency.

b. Sensitivity to vortex shape (outer decay length and inner power-law exponent)

Vortex shape is defined here by the power-law exponent inside the eye, n , and the outer decay length, X_1 . The maximum wind tendency is insensitive to changes in n when X_1 is at least 300 km (Fig. 10), and the fastest Exner function fall is more negative for larger X_1 because the gradient wind relation requires larger pressure falls to sustain stronger winds in a broader vortex. Because of increasingly negative $\partial v_0/\partial r$, leading to decreasing ζ_0 in the outer vortex, V_{\max} tendencies decrease as the vortex profile becomes sharper for $X_1 > 180 \text{ km}$.

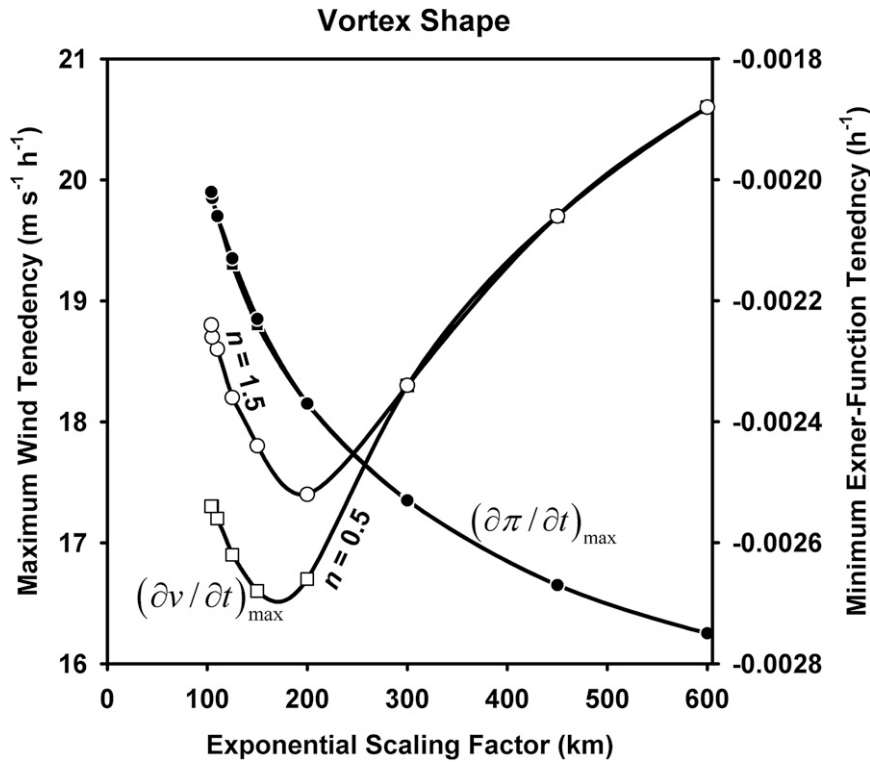


FIG. 10. Maximum rates of change of swirling wind and Exner function for $n = 0.5$ and 1.5 as X_1 varies from 104 to 600 km, where the calculations become unstable, in the idealized vortex.

Easier radial flow across the RMW into the inertially stiff eye causes $(\partial v_0/\partial t)_{\max}$ to increase when X_1 is <180 km. This effect is stronger for $n = 1.5$ because higher values of n produce a sharper vorticity maximum just inside the RMW. The variation of $(\partial v_0/\partial t)_{\max}$ is about $4 \text{ m s}^{-1} \text{ h}^{-1}$ over the range shape parameters explored here, compared with $23 \text{ m s}^{-1} \text{ h}^{-1}$ for the range of V_{\max} explored and about $10 \text{ m s}^{-1} \text{ h}^{-1}$ for the range of R_{\max} . The variation of maximum Exner function falls is less than 0.001 h^{-1} , compared with 0.004 h^{-1} over the ranges of R_{\max} and V_{\max} . Maximum Exner function falls are nearly identical for $n = 0.5$ and $n = 1.5$. Thus, the efficiency of TC intensification, as measured by $(\partial v_0/\partial t)_{\max}$ or $(\partial \pi/\partial t)_{\min}$ for fixed heating, is much less sensitive to vortex shape than it is to vortex size or intensity.

c. Heat source tilt and location

Aircraft observations (Jorgensen 1984) show that the outward slope of the 10-dBZ reflectivity boundary of the eyewall increases with R_{\max} and decreases with V_{\max} . We explore this effect by varying the tilts of two different heat sources, one in the eyewall and another that represents an outer convective ring 20 km outside it. Mean vortex structure is constant. The eyewall heat source produces significantly larger maximum wind

tendencies and Exner function falls because of smaller local Rossby radius (Fig. 11). It also causes instability for tilts ≥ 4 (where the tilt is the radial extent divided by the height of the heat source). Increasing tilt reduces the magnitude of both wind and Exner function tendencies because the induced flow becomes more nearly parallel to constant angular momentum surfaces. Since vertical eyewalls occur more often in stronger storms with relatively large updraft buoyancy, this effect should augment those of increasing V_{\max} and shrinking R_{\max} .

d. Vortex shape and heating location

The heating efficiency depends on the inertial stability in the neighborhood of the heat source. Figure 12 shows the combined sensitivity to forcing radius and different vortex shape parameters, n and X_1 . The vortex with $n = 1.5$ and $X_1 = 104$ km has the sharpest inertial stability gradients both inside and outside the eye.

For a fixed heating rate, the maximum wind tendency and Exner function fall are greatest when convective rings are closest to the center. In these calculations the horizontal inflow entering the eye crosses a tight gradient of angular momentum. As the heat source moves outward, the maximum tendencies drop rapidly until the heat source and RMW coincide and then decrease

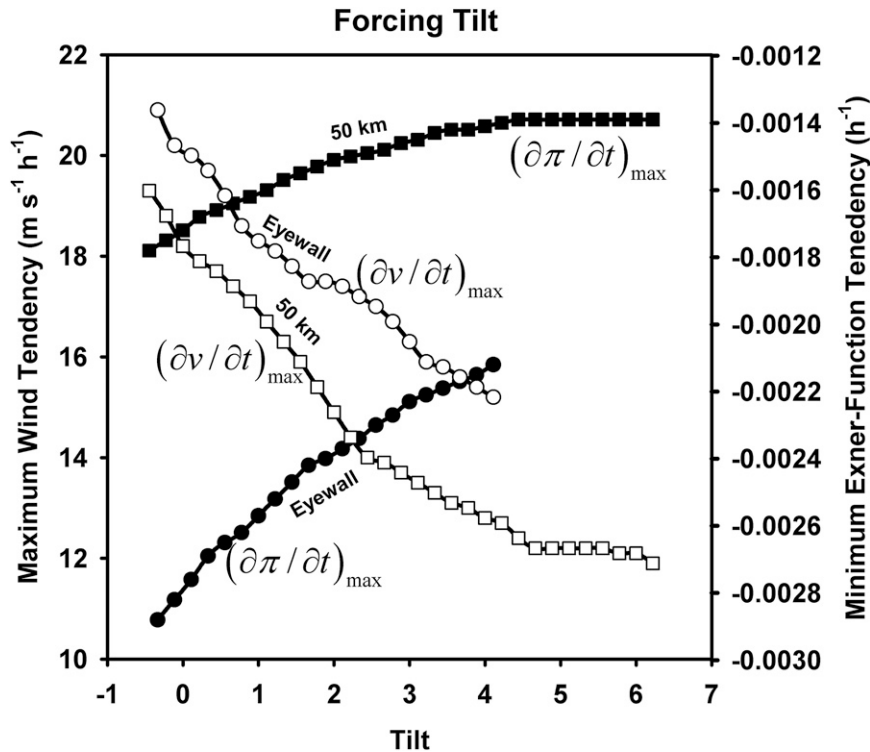


FIG. 11. Maximum rates of change of swirling wind and Exner function as a function of heat source tilt for forcing in the eyewall and 20 km outside the eyewall of the idealized vortex. In the eyewall tilt experiment, both the axis of the heat source and the RMW changed tilt together; but as the outer heat source tilted, the RMW retained the same inclination that it had in the standard vortex.

more slowly. The tendencies are greatest in the $n = 1.5$ vortex for heating inside the eye because it has the largest vorticity just inside the RMW; whereas the $X_1 = 300$ -km vortex has the greatest tendencies for heating outside the eye because it has the largest vorticity outside the RMW.

e. Surface friction

Inclusion of a frictional angular momentum sink makes the flow more complicated and realistic. Bulk aerodynamic surface friction forcing in the RV (Fig. 13; cf. Fig. 6) forces strong surface inflow. Since the SEQ is linear, the streamfunction is the superposition of Fig. 6 and a sharp near-surface gradient due to the frictional forcing (Fig. 13a). Convergent flow rises from the boundary layer (Fig. 13b) reversing weak thermally induced descent below 5–8-km altitude outside the eye in Fig. 6b. Consequently, only a thin layer of very weak sinking remains in the midtroposphere. An annulus of weak rising motion (around 10 cm s^{-1}) appears at 1-km altitude from the 50–90 km radius, which is near the location where outer convective rings often form. The forcing strengthens the surface inflow to 6 m s^{-1} (Fig. 13c). Outflow of more than 1 m s^{-1} fills much of the

lower troposphere between 2- and 4-km altitude beyond the 80-km radius. The only significant thermally induced inflow left surrounds the eyewall at 3–9-km altitude.

5. Discussion

The SEQ provides a perspective on some factors that control hurricane intensification in the context of balanced, symmetric vortices. The concept is not new (though this particular formulation has not been used before), but it is useful for TCs and has other applications, such as fronts. Other approaches to the intensification of hurricanes take into account important effects such as air–sea interaction and environmental factors. Although these factors are important, we do not explore them here. The oceanic sensible and latent heat sources determine how much energy is available to the storm. In contrast, here we take the heating as fixed and focus instead on the characteristics of the vortex (e.g., size, strength, shape) and the heat source geometry (e.g., tilt and location) that determine the efficiency of the vortex response. One observational study, Kaplan and DeMaria (2003), found no statistically significant relationship between hurricane intensity and RI, but did find that storms

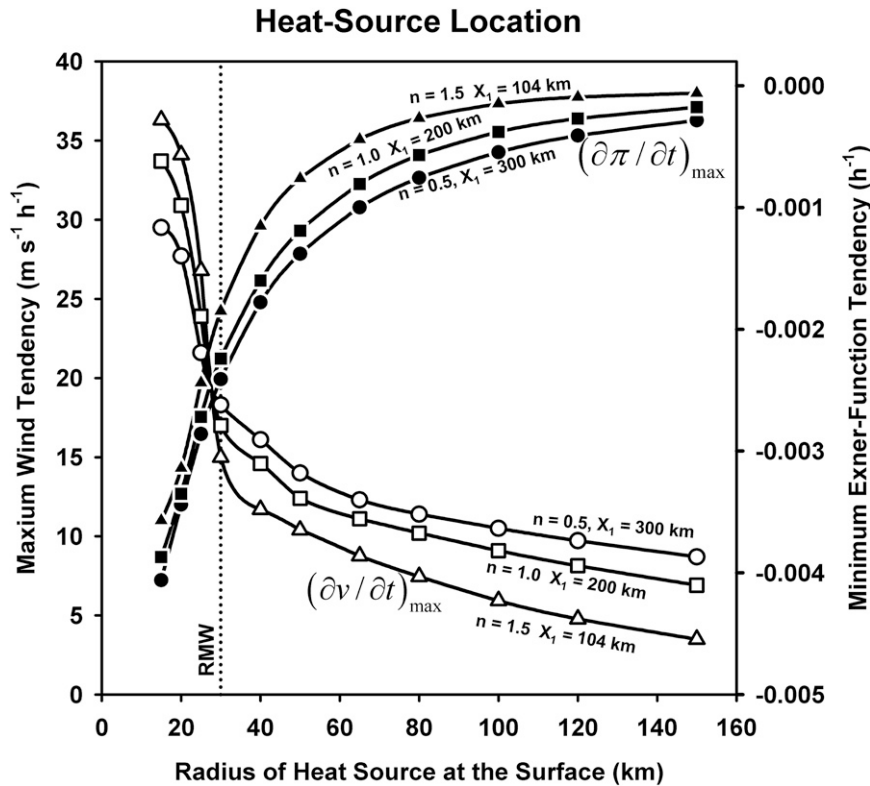


FIG. 12. Maximum rates to change of Exner function and swirling as a function of heat source radius for sharp ($n = 1.5$ and $X_1 = 104$ km), medium ($n = 1.0$ and $X_1 = 200$ km), and broad ($n = 0.5$ and $X_1 = 300$ km) vortex wind profiles.

underwent RI when they were far from their MPI. Their results emphasize the importance of thermodynamics.

The SEQ solutions can provide some insight into modeling. For example, Wang (2008) simulates the formation and maintenance of an annular hurricane, and hypothesizes that the tilt and radial location of the eyewall heating cause changes in the strength and location of the strongest mean tangential winds. Experiments designed to simulate different stages of Wang’s calculations explore these ideas with the SEQ. Positive values of $\partial v_0/\partial t$ at the RMW indicate intensification. Greater (lesser) values of $\partial v_0/\partial t$ inside the RMW, compared with the values outside, indicate contraction (expansion) of the eye.

In the early stage of annular hurricane development, the RMW is small and accompanied by a weak but developing outer heat source. As the heat source in SEQ simulations moves outward from the RMW, $\partial v_0/\partial t$ at the RMW decreases continuously. Tilting the outer heat source with a small RMW does not affect the RMW, but does affect the magnitude and vertical structure of outer swirling-wind tendencies. When the outer heat source is fixed and the RMW expands toward it, winds at the RMW decrease while winds outside the

RMW increase. However, the rates of change are slow compared with changes when the heat source is just inside the RMW. Ultimately, when the radius of the heat source and RMW both large, a steady state ensues. If the RMW and heat source are both held at a tilt of 1, the storm intensifies with no eye contraction or expansion, while greater (lesser) tilts show expansion (contraction). If the RMW and heat source tilts vary together, there is little expansion or contraction, only intensification. Increasing tilt decreases the magnitude of the intensification. Although more complex phenomena than are accounted for by the SEQ were probably important for the formation of annular hurricanes, tilts, and locations of heat sources and RMWs seem to be important for their maintenance.

6. Conclusions

Here we rederive the classical Sawyer–Eliassen equation in height coordinates and use a basic vortex that can be adjusted to represent a gamut of realistic primary-circulation structures. Height coordinates, combined with thermodynamics cast in terms of potential temperature and Exner function, add some complexity, but

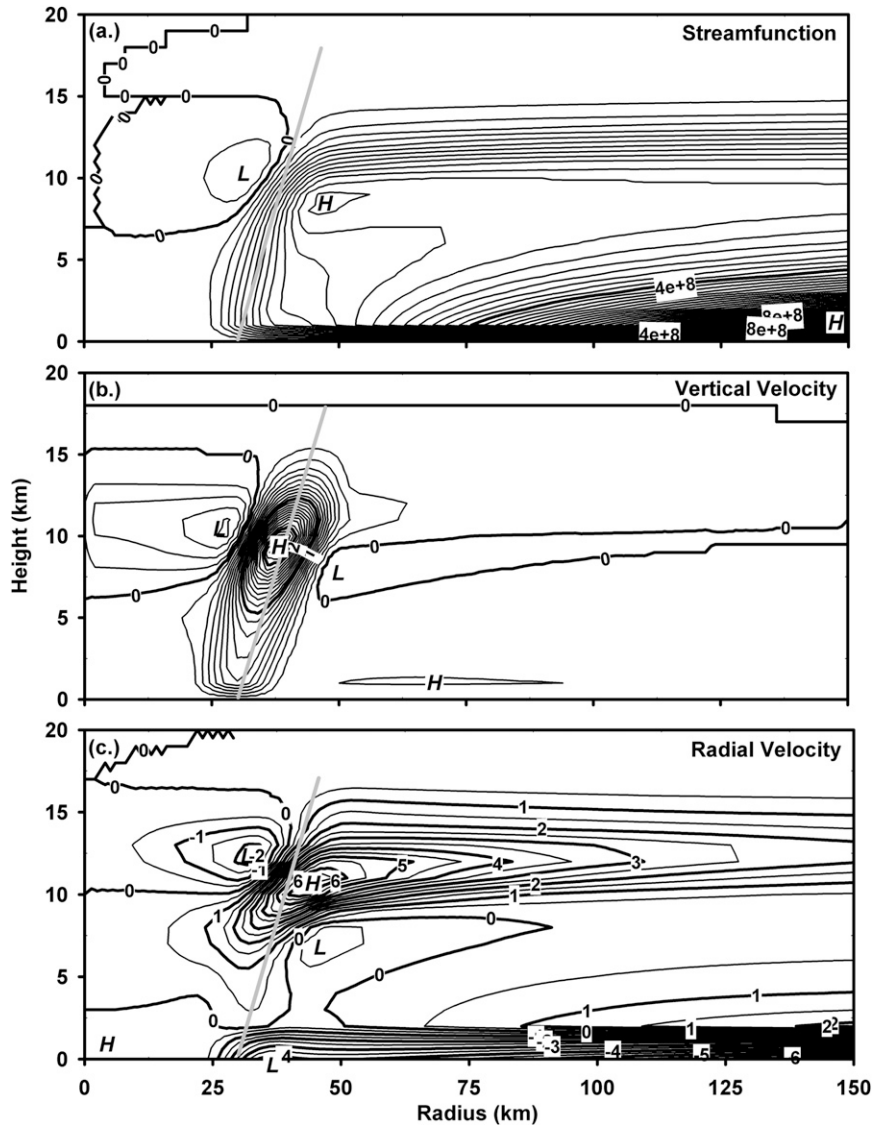


FIG. 13. Secondary circulation induced by the specified heat source combined with bulk aerodynamic surface friction acting on the realistic vortex: (a) mass-flow streamfunction (kg s^{-1}), (b) vertical velocity (m s^{-1}), and (c) radial velocity (m s^{-1}).

no more than does use of terrain-following vertical coordinates or interpolation to the surface in traditional pressure or log pressure vertical coordinates. The key advantage of height coordinates is that the horizontal sea surface—the locus of essential frictional and diabatic exchanges—is a coordinate surface.

We calculate secondary flows for both an idealized vortex with vertically constant shear, and a more realistic vortex where the lower troposphere is essentially barotropic and the shear is concentrated in the middle and upper troposphere. The former arrangement leads to somewhat reduced static stability (relative to the environmental sounding) throughout the vortex, but the

latter has increased static stability in the lower troposphere and significantly reduced stability in the upper troposphere. These variations change the character of the secondary flows by concentrating intensification near the surface in the idealized vortex and displacing it into the upper troposphere in the more realistic one. They also localize outflow from the eye of the realistic vortex to the midtroposphere where enhanced stability inhibits vertical motion. These results show that spatially varying stability consistent with the mean mass distribution is essential to simulation of realistic secondary flows. The present calculations confirm that increasing intensity and decreasing spatial scale, such that the scale

of the eye becomes comparable with the local Rossby radius of deformation, cause more of the energy released through heating to project onto vortex intensification. Greater intensity and smaller size are the most important parameters determining efficiency in converting latent heat to rotational kinetic energy as measured by the maximum $\partial v_0/\partial t$ anywhere in the domain.

The shape of the vortex, determined by a power-law exponent inside the eye and the exponential decay length outside the eye, and heat source tilt are less important by factors of 4–5. As in previous studies, the rate of intensification is sensitive to heat source position, becoming small when the strongest heating is far from the center and large when it is unphysically far inside the eye. Based on these results, we discount the seemingly plausible idea that variations in vortex profile shape, apart from changes in intensity or overall size, can predispose tropical cyclones to rapid intensification. A companion paper (Willoughby 2009) extends this analysis to heating that varies periodically with time.

Acknowledgments. AGP was supported by an NDSEG fellowship and an ARCS fellowship and HEW was supported by NSF Grant ATM-0454501.

REFERENCES

- AMS, 2007: Hurricane forecasting in the United States. *Bull. Amer. Meteor. Soc.*, **88**, 950–953.
- Bister, M., and K. Emanuel, 1998: Dissipative heating and hurricane intensity. *Meteor. Atmos. Phys.*, **65**, 233–240.
- Emanuel, K., 2004: Tropical cyclone energetic and structure. *Atmospheric Turbulence and Mesoscale Meteorology: Scientific Research Inspired by Douglas Lilly*, E. Fedorovich, R. Rotunno, and B. Stevens, Eds., Cambridge University Press, 165–192.
- Jorgensen, D. P., 1984: Mesoscale and convective-scale characteristics of mature hurricanes. Part II: Inner core structure of Hurricane Allen (1980). *J. Atmos. Sci.*, **41**, 1287–1311.
- Kaplan, J., and M. DeMaria, 2003: Large-scale characteristics of rapidly intensifying tropical cyclones in the North Atlantic basin. *Weather Forecasting*, **18**, 1093–1108.
- La Seur, N. E., and H. F. Hawkins, 1963: An analysis of Hurricane Cleo (1958) based on data from research reconnaissance aircraft. *Mon. Wea. Rev.*, **91**, 694–709.
- Lindzen, R. S., and H. L. Kuo, 1969: A reliable method for the numerical integration of a large class of ordinary and partial differential equations. *Mon. Wea. Rev.*, **97**, 732–734.
- Marks, F. D., and R. A. Houze, 1987: Inner core structure of Hurricane Alicia from airborne Doppler-radar observations. *J. Atmos. Sci.*, **44**, 1296–1317.
- Ooyama, K., 1969: Numerical simulation of the life cycle of tropical cyclones. *J. Atmos. Sci.*, **26**, 3–40.
- , 1982: Conceptual evolution of the theory and modeling of the tropical cyclone. *J. Meteor. Soc. Japan*, **60**, 369–380.
- Pearce, R. P., 2004: An axisymmetric model of a mature tropical cyclone incorporating azimuthal vorticity. *Quart. J. Roy. Meteor. Soc.*, **130**, 259–293.
- Roux, F., and N. Viltard, 1995: Structure and evolution of Hurricane Claudette on 7 September 1991 from airborne Doppler radar observations. Part I: Kinematics. *Mon. Wea. Rev.*, **123**, 2611–2639.
- Schubert, W. H., and J. J. Hack, 1982: Inertial stability and tropical cyclone development. *J. Atmos. Sci.*, **39**, 1687–1697.
- , C. M. Rozoff, J. L. Vigh, B. D. McNoldy, and J. P. Kossin, 2007: On the distribution of subsidence in the hurricane eye. *Quart. J. Roy. Meteor. Soc.*, **133**, 595–605.
- Shapiro, L. J., and H. E. Willoughby, 1982: The response of balanced hurricanes to local sources of heat and momentum. *J. Atmos. Sci.*, **39**, 378–394.
- Sheets, R. C., 1969: Some mean hurricane soundings. *J. Appl. Meteor.*, **8**, 134–146.
- Smith, R. K., 1981: The cyclostrophic adjustment of vortices with application to tropical cyclone modification. *J. Atmos. Sci.*, **38**, 2021–2030.
- , 2003: A simple model of the hurricane boundary layer. *Quart. J. Roy. Meteor. Soc.*, **129**, 1007–1027.
- , 2006: Accurate determination of a balanced symmetric vortex in a compressible atmosphere. *Tellus*, **58A**, 98–103.
- , M. T. Montgomery, and H. Zhu, 2004: Buoyancy in tropical cyclones and other rapidly rotating vortices. *Dyn. Atmos. Oceans*, **40**, 189–208.
- Viltard, N., and F. Roux, 1998: Structure and evolution of Hurricane Claudette on 7 September 1991 from airborne Doppler radar observations. Part II: Thermodynamics. *Mon. Wea. Rev.*, **126**, 281–302.
- Wang, Y., 2008: Structure and formation of an annular hurricane simulated in a fully compressible, nonhydrostatic model—TCM4. *J. Atmos. Sci.*, **65**, 1505–1527.
- Willoughby, H. E., 1990a: Temporal changes of the primary circulation in tropical cyclones. *J. Atmos. Sci.*, **47**, 242–264.
- , 1990b: Gradient balance in tropical cyclones. *J. Atmos. Sci.*, **47**, 265–274.
- , 1998: Tropical cyclone eye thermodynamics. *Mon. Wea. Rev.*, **126**, 3053–3067.
- , 2009: Diabatically induced secondary flows in tropical cyclones. Part II: Periodic forcing. *Mon. Wea. Rev.*, **137**, 822–835.
- , J. A. Clos, and M. B. Shoreibah, 1982: Concentric eyewalls, secondary wind maxima, and the development of the hurricane vortex. *J. Atmos. Sci.*, **39**, 395–411.
- , R. W. R. Darling, and M. E. Rahn, 2006: Parametric representation of the primary hurricane vortex. Part II: A new family of sectionally continuous profiles. *Mon. Wea. Rev.*, **134**, 1102–1120.
- , E. N. Rappaport, and F. D. Marks, 2007: Hurricane forecasting: The state of the art. *Nat. Hazards Rev.*, **8**, 45–49.
- Zhang, D.-L., Y. Liu, and M. K. Yau, 2000: A multiscale numerical study of Hurricane Andrew (1992). Part III: Dynamically induced vertical motion. *Mon. Wea. Rev.*, **128**, 3722–3788.